Supporting Information

Synergetic Effects of Dual Electrocatalysts for High-Performance Solar-Driven Water Oxidation

Rajender Boddula,†,|| Beidou Guo,†,‡,|| Akbar Ali,†,‡,|| Guancai Xie,†,‡ Yawen Dai,†,‡ Chang Zhao,†,‡ Yuxuan Wei,†,‡ Saad Ullah Jan,†,‡ and Jian Ru Gong*,†,‡

[†]Chinese Academy of Sciences (CAS) Center for Excellence in Nanoscience, CAS Key Laboratory of Nanosystem and Hierarchy Fabrication, National Center for Nanoscience and Technology, Beijing 100190, China

‡University of CAS, Beijing 100049, China

*Email: gongjr@nanoctr.cn

This file includes:

Figure S1 to S16 Table S1 to S8

Device fabrication

The commercial polycrystalline n⁺p-Si photoabsorbers were purchased from LDK Solar Co. Ltd., the bared p-type side for integration with catalysts having an anti-reflection layer on the n⁺-Si emitter layer and then as-received substrate was cleaved into the required pieces (1 cm × 1 cm) and were rinsed with acetone, isopropyl alcohol and deionized water (DI water, Milli-Q 18.2 M Ω .cm) with ultrasonic agitation, each for 5 min, in succession. Immediately prior to metal (Fe, Co, Ni) film coating, the p-side of the n⁺p-Si junction was etched in buffered HF (10% in volume) for 20 s (the emitter side was protected by the SiN_x layer), rinsed with DI water, dried with N₂ gas, fixed on the sample holder using the Kapton tape and open the buried n⁺p-Si junction, finally loaded into the vacuum chamber of the thermal evaporation system (ZHD-300, Technol Science Co., Ltd) for metal film deposition for required thickness at the rate of $\sim 0.1~\text{Å s}^{-1}$, keeping the Si substrate temperature at 150 °C. Thermal deposition of metal on the p-side surface of n+p-Si, the silver electrodes at the emitter side were adhered to the transparent indium-doped tin oxide (ITO) coated conducting glass, which acts as a transparent conductor for the PEC test, supports and protects the emitter against contacting with solution, by rubbing the indium-gallium (InGa) eutectic. To prepare the electrodes, one strip of the copper tape was inserted into a polytetrafluoroethylene tube, and the other strip was fixed on the outer wall of this tube. The two strips of the copper tapes were adhered to the ITO glass and metal film by InGa, as the electrical wires of working electrodes for PEC test and electrodeposition of FeOOH, respectively. After that, the entire assembly was encased by epoxy (Hysol 9460F) to avoid the leakage of electrolyte and using 704 silica gel was used as a second protecting layer on epoxy. The free ends of these two strips of the copper tapes were used to connect power source to apply the external voltage.

The M (= Fe, Co, Ni) metal film on the n⁺p-Si/SiO_x/M photoelectrode was activated by cycling the potential between -0.3 to 1.6 V versus saturated calomel electrode (SCE) using cyclic voltammetry (CV) in 1.0 M KOH electrolyte by twenty consecutive CV scans at the sweep rate of 50 mV s⁻¹, using Zahner Zennium electrochemical workstation and a Pt sheet as a counter electrode, SCE as a reference electrode and n⁺p-Si/SiO_x/M as a working electrode, under 1 Sun.

Finally, FeOOH film was electrodeposited¹ on the n⁺p-Si/SiO_x/aM film by facile cathodic-electrodeposition approach using electrochemical workstation (CHI760E, Germany) in a three-electrode system, using the interlayer film as the working electrode, Pt sheet as the counter electrode and saturated-calomel electrode (SCE) as the reference electrode by applying cathodic potential of -1.0 V in electrolyte containing 30 mM ferric nitrate [Fe(NO₃)₃·9H₂O] (99.999 %, Guanghua) for different periods (100 to 500 s). All the electrochemical depositions were carried out by applying the cathodic potential of -1.0 V versus SCE in the dark.

Control samples prepared by electrodeposition of $Ni_{1-x}Fe_xOOH$ on the n^+p-Si/SiO_x was optimized by regulation the Ni^{2+} and Fe^{3+} ions content ratio in precursor solution and total amount of ions was kept to 30 mM in 100 ml of aqueous solution by applying the cathodic potential of -1.0 V versus SCE in the dark.

All of the electrodes were $\sim 1~\rm cm^2$ in area unless specified otherwise. To assure the reproducibility of the results, at least fifteen electrodes of each type were fabricated and tested in this work. All electrodes show similar characteristics and activity, and the representative data are reported.

Characterization

Scanning electron microscopy (SEM) images and Energy dispersive spectroscopy (EDS) elemental mapping images were obtained from high-resolution field-emission S4800 scanning electron microscope (FESEM, Hitachi, Japan) at an accelerating voltage of 10 kV. High-resolution EDS elemental mapping images were obtained by a field-emission transmission electron microscope (FEI Titan G2 60-300) operated at 200 kV under the mode of high-resolution transmission electron microscopy (HRTEM) is equipped with a high-brightness field emission gun (X-FEG), a monochromator unit, a probe and image spherical aberration (Cs) corrector and a super-X EDXS system equipped with HAADF detector. The concentration of Ni²⁺ and Fe³⁺ ions deposition in the electrolyte solution were determined by inductively coupled plasma-atomic emission spectroscopy (ICP-AES) with a Shimazu ICPS-8100 sequential type ICP emission spectrometer. X-ray photoelectron spectra (XPS) measurements carried out by ultrahigh vacuum VG ESCALAB 210 electron spectrometer equipped with a

multi-channel detector. The spectra were excited using monochromatic Al K α (1486.6 eV) source radiation. The baseline of XPS spectra is Shirley fitted by XPS peak fit software.

PEC measurements

electrochemical and photoelectrochemical measurements were studied on an electrochemical workstation (Zahner zennium, Germany) with a three-electrode system in 1.0 M KOH (pH=13.6) electrolyte at the sweep rate of 50 mV s⁻¹, with a Pt sheet as a counter electrode, SCE as a reference electrode and n+p-Si/SiO_x/aM:FeOOH as a working electrode, under irradiation with simulated air mass 1.5 global (AM 1.5G) sunlight generated from a 500 W Xenon lamp equipped with an AM 1.5G filter (CEL-S500, Au-light Co., Ltd.), and the light density was calibrated to be 100 mW cm⁻² (1 Sun). All measured potentials were converted to the RHE reference scale using the following relationship: $E_{RHE} = E_{SCE} + 0.244 \text{ V} + 0.059 \times \text{pH}$. Cyclic voltammetry (CV) measurements were recorded between 0.5 and 2.4 V versus RHE in 1 M KOH. Chronoamperometric measurements were recorded at the applied potential of $1.0V_{\rm RHE}$. n+p-Si/SiO_x/M electrodes were activated by 20 CV sweep cycles at the scan rate of 50 mV s⁻¹. The photovoltage (V_{ph}) of the photoanode was determined by the potential difference between the catalyst layer coated on n+p-Si/SiO_x under irradiation and on metallic p++-Si/SiO_x²⁻⁴ in the dark at 5 mA cm⁻². Since the coated catalyst is same on the metallic p⁺⁺-Si/SiO_x and n⁺p-Si/SiO_x, the J-V curve shift is caused by the thermodynamic contribution, that is, the effect of generated photovoltage under irradiation. Oxygen was determined through operation in a three-electrode system in a closed configuration at a potential of 1.23 $V_{\rm RHE}$ in which the photoelectrochemically produced oxygen gases were analyzed by a gas chromatograph (GC, 9790II) with thermal conductivity detector (TCD). The applied bias photon-to-current efficiency (ABPE) of the photoanode measured on the current density versus potential (J-V) curve under irradiation.² Electrochemically active surface area (ECSA) was determined by measuring the capacitive current associated with double-layer charging from the scan rate dependence of CVs. ECSA was measured on the same with CV potential window of 0.2-0.3 V versus SCE in 1 M KOH. The scan rates were 20, 40, 60, 80 and 100 mV sec⁻¹. The double-layer capacitance (C_{dl}) was estimated by plotting the current density (j_a-j_c) at 0.25 V versus SCE against the scan rate. The slope is twice of the double-layer capacitance (C_{dl}) and equal to the ECSA. Electrochemical impedance spectroscopy (EIS) measurement were recorded at 1.23 $V_{\rm RHE}$ in the frequency range of 0.1 Hz-100 KHz and this impedance data are presented in the form of Nyquist plot. The values of the charge transfer resistance ($R_{\rm ct}$) of the photoelectrodes were determined by Zsimpwin software simulations.

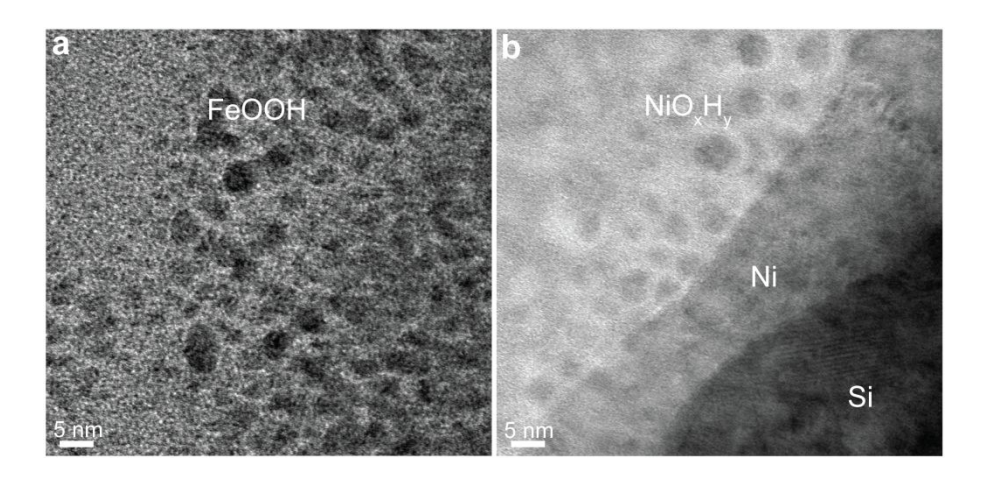


Figure S1. The cross-sectional HRTEM image of $n^+p-Si/SiO_x/aNi$:FeOOH for more clear morphology and microstructure of Figure 1c.

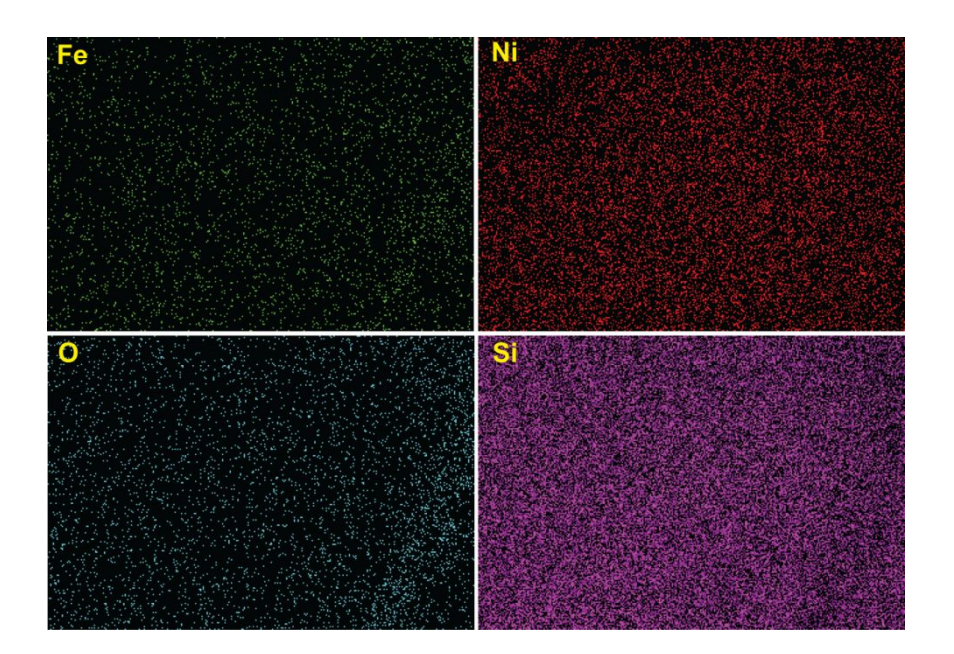


Figure S2. EDS elemental mapping images of n⁺p-Si/SiO_x/aNi:FeOOH, showing that the Ni, Fe, and O elements are uniformly distributed on the Si substrate.

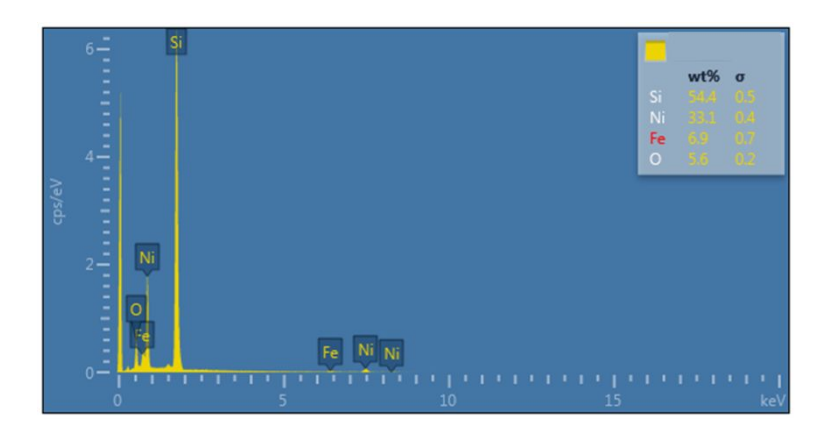


Figure S3. The corresponding EDS spectrum of n^+p -Si/SiO_x/aNi:FeOOH, indicating Ni, Fe, O, and Si elements are present in the electrode.

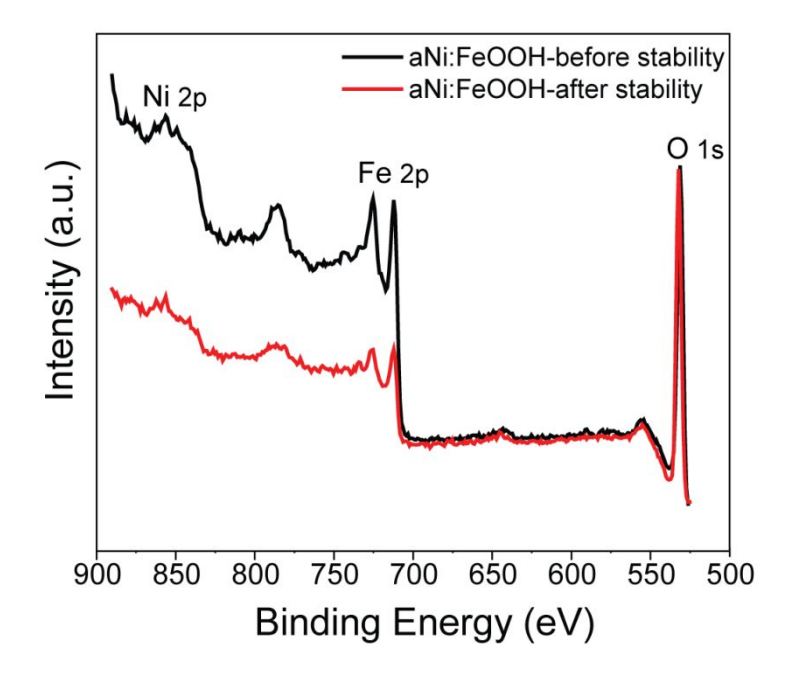


Figure S4. XPS survey spectra before and after the stability test of the n^+p -Si/SiO_x/aNi:FeOOH photoanode, confirming the existence of Fe, Ni, and O elements.

Table S1. Surface atomic ratios (%) of XPS detected elements in n⁺p-Si/SiO_x/aNi:FeOOH before and after the stability test

Atomic ratio	Fe (%)	Ni (%)	O (%)	C (%)
Before stability	14.57	1.34	45.78	38.40
After stability	5.02	1.18	43.53	40.27

The valence states of Fe and Ni after the stability test are basically the same as those before the stability test. The Ni:Fe ratio in n⁺p-Si/SiO_x/aNi:FeOOH increases from 8:92 to 19:81 after the 110 h stability test compared to that before the stability test.

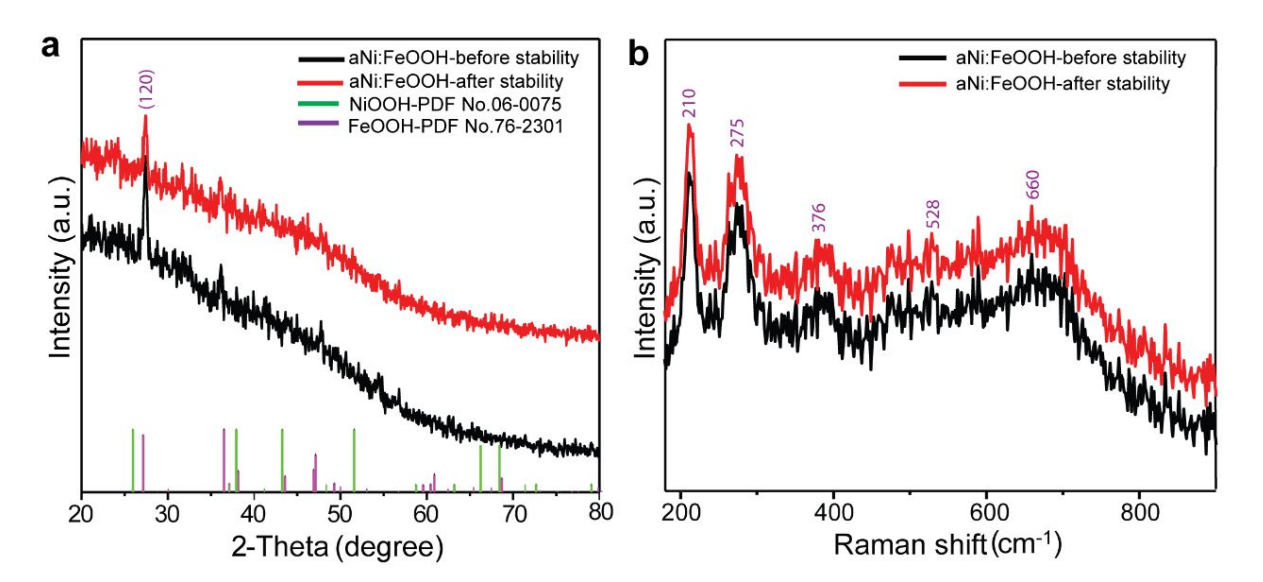


Figure S5. (a) XRD and (b) Raman spectra of the n^+p -Si/SiO_x/aNi:FeOOH photoanode before and after the stability test.

Before the stability test, the XRD pattern of the n^+p -Si/SiO_x/aNi:FeOOH anode exhibits a diffraction peak at 27.4°, which is assigned to the (120) crystal-plane reflection of orthorhombic lepidocrocite (γ -FeOOH) phase (PDF Card No. 76-2301) (Figure S5a), in accordance with previously reported metal oxyhydroxides.¹ The Raman spectrum of this anode shows several weak broad peaks at around 210, 275, 376, 528, and 660 cm⁻¹, which can

be attributed to M-O and M-OH vibrations of metal oxyhydroxides (Figure S5b), in good agreement with the Raman spectroscopy characteristics of γ -FeOOH reported in the literature.^{5–7} Hence, both XRD and Raman characterizations confirm that γ -FeOOH exists on the n⁺p-Si/SiO_x/aNi:FeOOH photoanode surface layer. The similar XRD and Raman spectra of the n⁺p-Si/SiO_x/aNi:FeOOH anode is observed after the PEC stability test, displaying the robust electrode structure. No NiOOH signal is observed in both XRD and Raman spectra, which might be due to the small amount of NiOOH in the top layer.

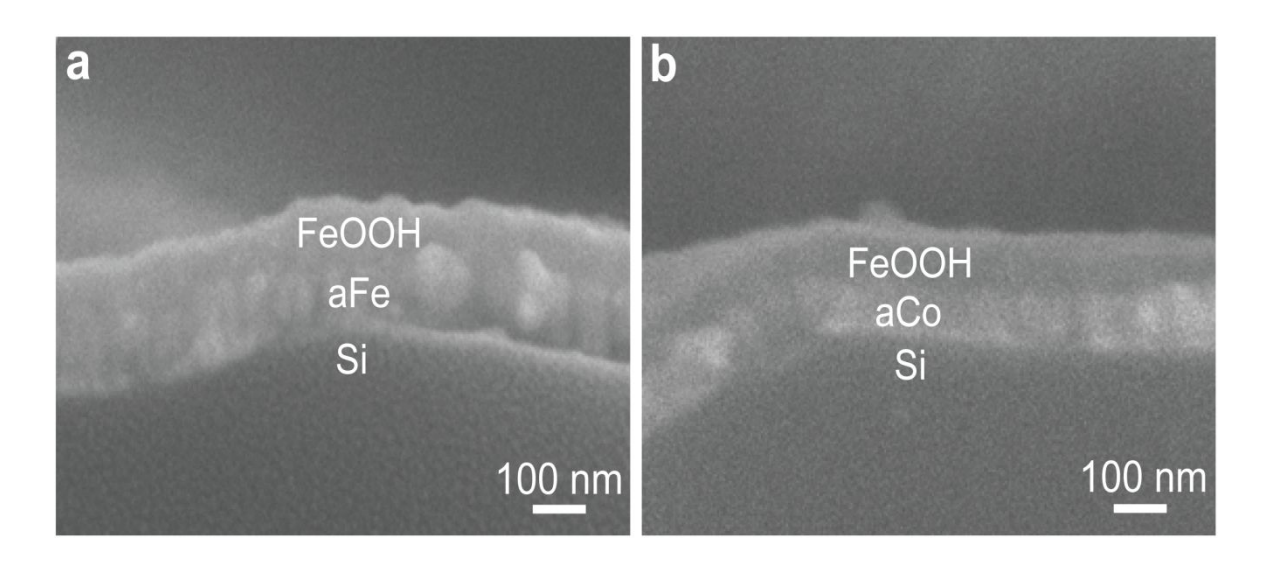


Figure S6. The cross-sectional SEM images of the (a) $n^+p-Si/SiO_x/aFe$:FeOOH and (b) $n^+p-Si/SiO_x/aCo$:FeOOH photoanodes.

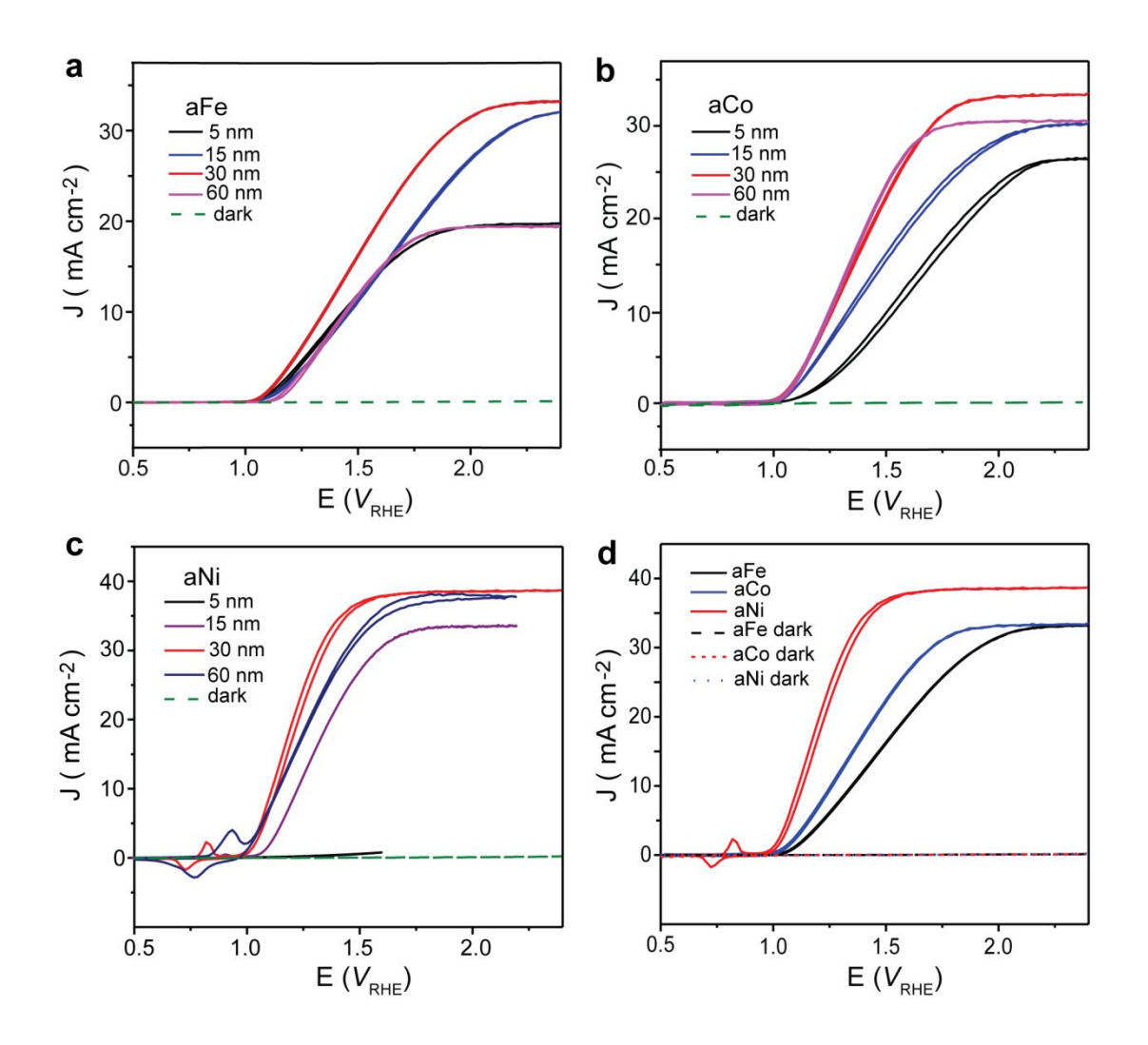


Figure S7. (a-c) The metal film thickness-dependent OER activity of the n^+p -Si/SiO_x/aM (M = Fe, Co, Ni) photoanodes in 1 M KOH electrolyte at the scan rate of 50 mV s⁻¹ under irradiation of 100 mW cm⁻² (AM 1.5 G); (d) comparison of the n^+p -Si/SiO_x/aM (M=Fe, Co, Ni) photoanodes with an optimized thickness obtained from (a-c).

The metal film thickness-dependent PEC activity of the n⁺p-Si/SiO_x/aM (M=Fe, Co, Ni) photoanodes demonstrate that the 30 nm Fe, Co, Ni metal film thickness corresponds to the best PEC performance with the lowest onset potential and the highest saturated photocurrent density, respectively (Figure S7a-c, Tables S2-S4). The comparison of the n⁺p-Si/SiO_x/aM (M=Fe, Co, Ni) photoanodes with an optimized thickness shows that the n⁺p-Si/SiO_x/aNi anode with a 30 nm metal Ni thickness has the highest OER activity (Figure S7d, Table S5).

Table S2. OER activity comparison before and after activation for $n^+p-Si/SiO_x/aFe$ with varying thicknesses of the metal Fe film

Fe thickness (nm)	Onset potential $(V_{ m RHE})$		Photocurre at 1.23 V _{RF} (mA cm ⁻²)	•	Saturation photocurrent density (mA cm ⁻²)		
	before activation			after activation	before activation	after activation	
5	1.06	1.05	3.10	3.93	19.71	19.45	
15	1.06	1.04	3.14	4.30	31.08	32.27	
30	1.05	1.03	4.00	5.63	33.43	33.43	
60	1.12	1.10	2.50	2.93	19.45	19.45	

Table S3. OER activity comparison before and after activation for $n^+p-Si/SiO_x/aCo$ with varying thicknesses of the metal Co film

Co thickness (nm)	Onset potential $(V_{ m RHE})$		Photocurro at 1.23 V _{RE} (mA cm ⁻²)	•	Saturation photocurrent density (mA cm ⁻²)		
	before activation	after activation	before activation	after activation	before activation	after activation	
5	0.99	0.99	2.42	4.33	26.89	26.43	
15	1.01	0.98	6.51	6.97	30.18	30.46	
30	1.00	0.99	8.77	9.60	30.17	34.11	
60	0.95	0.94	10.09	9.10	33.38	33.39	

Table S4. OER activity comparison before and after activation for $n^+p-Si/SiO_x/aNi$ with varying thicknesses of the metal Ni film

Ni thickne ss (nm)	Onset potential $(V_{\rm RHE})$		Photocur density at $V_{\rm RHE}$ (mA cm ⁻²)	1.23	Saturation photocurrent density (mA cm ⁻²)		
	Before activatio	After activatio	Before activatio	After activatio	Before activatio	After activatio	
	n	n	n	n	n	n	
5			0	0.15	0	0.7	
15	1.23	1.02	7.0	11.24	30.2	33.62	
30	0.99	0.96	19.73	22.32	31.17	38.55	
60	1.02	0.99	10.5	17.72	35.38	37.68	

Table S5. OER activity comparison of the n^+p -Si/SiO_x/aM (M=Fe, Co, Ni) photoanodes with the optimized metal film thickness

Metal thickness (30 nm)	Onset potential $(V_{ m RHE})$	Photocurrent density at 1.23 $V_{\rm RHE}$ (mA cm ⁻²)	Saturation photocurrent density (mA cm ⁻²)
Fe	1.03	5.63	33.43
Co	0.99	9.60	34.11
Ni	0.96	22.32	38.55

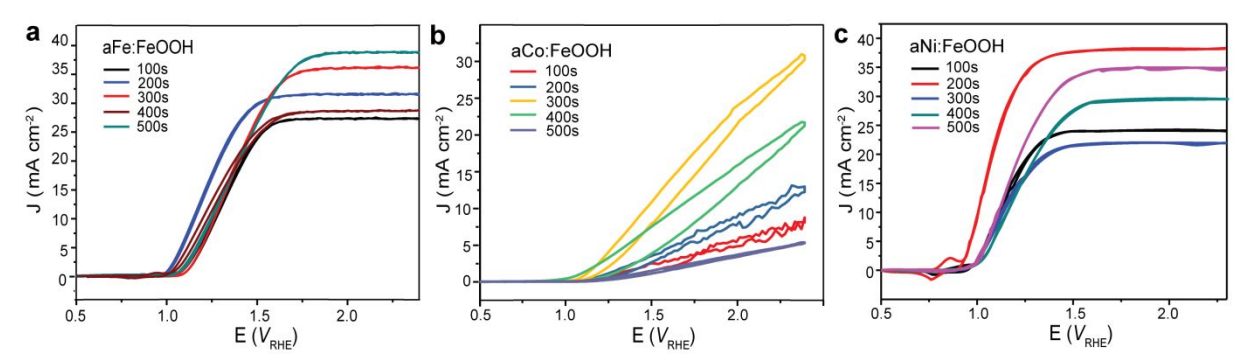


Figure S8. FeOOH electrodeposition time-dependent OER performances of the n⁺p-Si/SiO_x/aM:FeOOH (M=Fe, Co, Ni) photoanodes with the optimized metal film thickness of 30 nm. FeOOH electrodeposition durations: 100, 200, 300, 400, and 500 s. FeOOH electrodeposition conditions: 30 mM of ferric nitrate aqueous solution at the applied cathodic potential of -1.0 V versus SCE.

200s electrodeposition of FeOOH is chosen as the optimized parameter for n⁺p-Si/SiO_x/aM:FeOOH (M=Fe, Co, Ni) photoanodes.

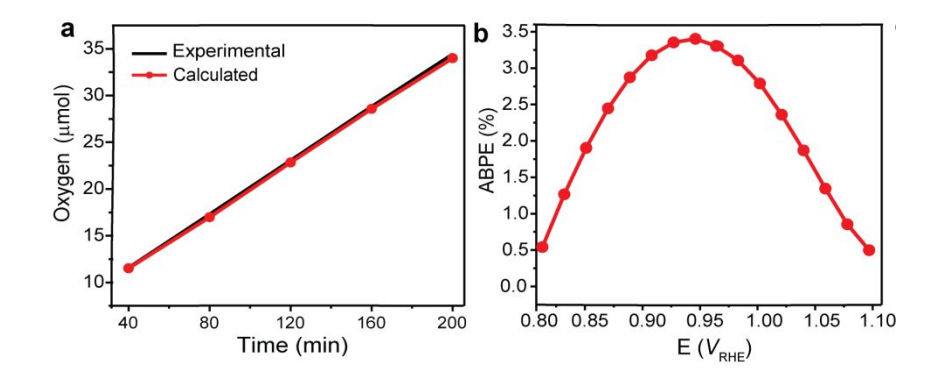


Figure S9. (a) O₂ production measured for the n⁺p-Si/SiO_x/aNi:FeOOH photoanode under irradiation in 1.0 M KOH (red line) and calculated based on the charge passed assuming 100% Faradaic efficiency (black line), (b) ABPE of the n⁺p-Si/SiO_x/aNi:FeOOH photoanode.

The Faradaic efficiency evaluated by comparing the photocurrent to the actual O_2 yield and theoretical O_2 production is ~100%, suggesting the efficient water splitting during the PEC OER (Figure S9a). Based on the 100% Faradaic efficiency, the applied bias photon-to-current efficiency (ABPE, also called the ideal solar-to- O_2 conversion efficiency) of this photoelectrode is calculated to be 3.4% at 0.95 $V_{\rm RHE}$ (Figure S9b).

Table S6. OER performance comparison of Si-based photoanodes

Photoanode	Onset potential (V _{RHE})	Photocurrent at water oxidation potential (mA cm ⁻²)	Saturation photocurrent density (mA cm ⁻²)	Stability	Photo voltage (mV)	Fabrication method	Irradiation conditions	Ref.
n ⁺ p-Si/SiO _x /aNi:FeOOH	0.91	33.20	38.5	110 h/ 1 M KOH	610	Successive CV potential cycling & Electrodeposition	AM 1.5 G (1-sun)	This work
n+p-Si/SiO ₂ /aNi/NiFe-LDH	0.79 ± 0.02	37.73	41.3	68 h/1 M KOH	608	Successive CV potential cycling & Electrodeposition	AM 1.5 G (1-sun)	4
Si/Graphene/TiO ₂ /FeNiCo O _x	1	~7	~19	6 h/1M NaOH	420	CVD, ALD, spin coating	AM 1.5 (100 mW cm ⁻²)	8
n ⁺ p-Si/SiO ₂ /NiFe Alloy	0.89	30.7	30.7	13 h/1 M KOH	620	Electrodeposition	1-sun simulated solar	9
n-Si/Ni NPs	1.1	~3.5	33	10 h/1 M NaOH	500	Electrodeposition	AM 1.5 G	10
$Ni_{80}Fe_{20}/TiO_2/n$ -Si	1.06	21.5	33	10 h/1 M KOH	500	Electrodeposition	AM 1.5 G	11
n-Si/SiO _x /Al ₂ O ₃ /Pt/Ni	0.997	19.2	28.5	200 h/1 M KOH	490	ALD & RF sputtering	Simulated AM 1.5 solar (100 mW cm ⁻²)	12
n-Si/GO/CNTs/Graphene	~ 1.23	1	8	17 min/1 M KOH 6 days	-	Langmuir-Blodg ett	AM 1.5 (1-sun)	13
$n^+pp^+/Si/Co/NiCoO_x$	~1	21	21	after 72h stabilizat ion in activity/ 1 M KOH	510	Sputtering	AM 1.5 $G/\lambda > 635$ nm)/ 1000 W Xe Lamp	14
$n^+p\text{-Si/SiO}_2/\text{TiO}_2/\text{Ir}$	~0.95	~2.6	-	-	630	ALD	AM 1.5 G (1-sun) simulated solar AM 1.5 G	15
n-Si/CoO _x	1.024 ± 0.2	22.9 ± 1.6	27	2500 h/1 M KOH	570	ALD	(1-sun) G/100 W Xe Lamp AM 1.5 G	2
Co ₃ O ₄ /CoO/SiO _x /Si	~1	3.5	32.5	12 h/1 M KOH	480	ALD	(1-sun) /300 W Xe	3
$p^{\scriptscriptstyle +} n\text{-}Si/CoO_x$	1	17	30	24 h/1 M KOH	610	Plasma enhanced ALD	Lamp (1-sun)/ 150 W Xe Lamp AM 1.5 G	16
np ⁺ -Si/NiCo ₂ O ₄ /NiFe	0.95	>25	33	72 h/1 M KOH	-	Reactive sputtering	(1-sun) simulated solar	17
n-Si/SiO _x /Co/CoOOH	~1.52	0	35	2 h	470	Electrodeposition	Simulated AM 1.5G	18

n-Si/SiO ₂ /Ni/NiO _x	~1.07	12	~56	12 h/1 M KOH	500	Electron beam evaporation	AM 1.5 G (2-sun) /150 W Xe	19
np+-Si/NiO _x	1.05 ± 0.2	29 ± 0.8	~33	1200 h/1 M KOH	-	Sputtering	Lamp AM 1.5 G (1-sun)	20
np ⁺ -Si/NiO _x	0.95	20.7 ± 5	29	~36 h/1 M KOH	-	Sputtering	(1-sun) simulated solar	21
p+n-Si/Iron treated NiO	1.05	~16.5	~19	300 h/1 M KOH	500	Sputtering	38.6 mW/cm ² / λ >635 nm)	22
NiO _x /Ni/n-Si	1.08	14.7	31.7	~7 h / 1 M NaOH	~500	Pulsed electrodeposition & post-annealing	1 sun (AM 1.5G, 100 mW cm ⁻²)	23
Ni/n-Si	1.09	8.86	27.5	24 h / 1 M KOH	470	Electroless deposition	1 sun (AM 1.5G, 100 mW cm ⁻²)	24
np ⁺ -Si/TiO ₂ /Ni	~1	~13	33.6	>100 h/1 M KOH	520	ALD	AM 1.5 G (1-sun) /100 W Xe	25
$p^+ n \text{-Si/Ir/IrO}_2$	0.93	13.8	23	18 h/1 M H ₂ SO ₄	500	Sputtering	Arc Lamp 38.6 mW/cm ² /λ >635 nm)/ 150 W Xe Lamp	26
Si/SiO ₂ /TiO ₂ /Ir	~1.03	~16	~26	8 h/1mA cm ⁻² /1 M NaOH	~550	ALD	AM 1.5 G (1-sun) simulated solar	27
n-Si/NiFe-2nm	1.09	25.2	32	50 h/1 M NaOH	461	Thermal evaporation	AM 1.5G (100 mW cm ⁻²)	28
n-Si/SiO _x /SnO _x /Ni	0.91	30.8	31.5	25 h/ 1 M KOH	620	Spray deposition & sputtering	AM 1.5G (100 mW cm ⁻²)	29
n-Si/ZrO ₂ /NiFe	0.96	26.6	36.4	100 h	505	ALD & e-beam evaporation	AM 1.5G (100 mW cm ⁻²)	30

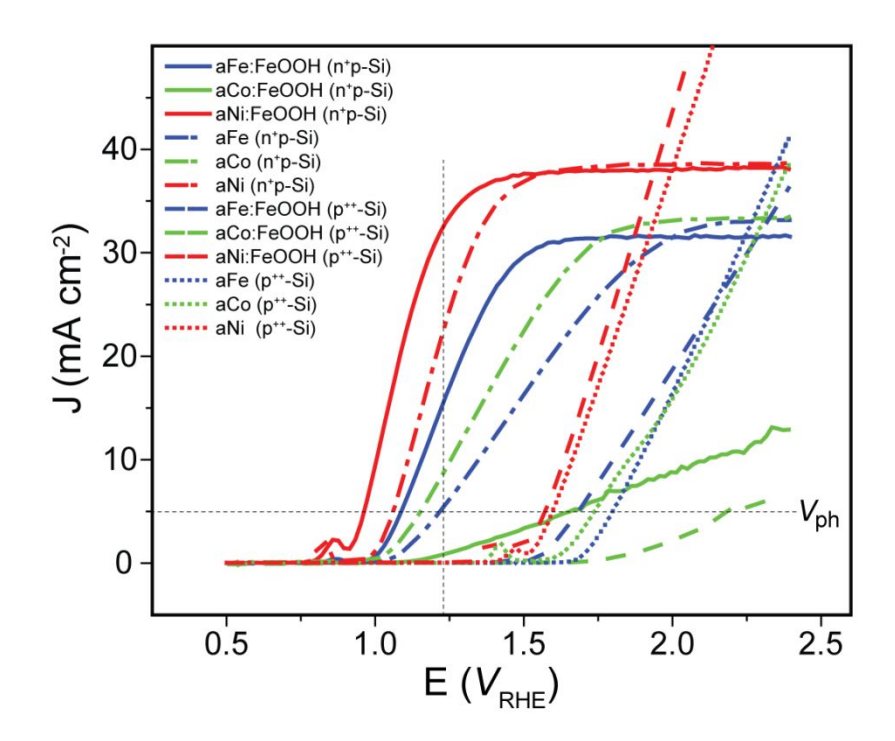


Figure S10. J-V behavior of aM:FeOOH (solid curves) and aM (dash-dot curves) coated on n^+p -Si/SiO_x photoanodes under irradiation of 100 mW cm⁻² (AM 1.5 G) and aM:FeOOH (dashed curves) and aM (dotted curves) coated on p^{++} -Si/SiO_x electrodes in the dark in 1 M KOH electrolyte at the scan rate of 50 mV s⁻¹. The photovoltage (V_{ph}) of the photoanode is determined by the potential difference between the catalyst layer coated on n^+p -Si/SiO_x under irradiation and on metallic p^{++} -Si/SiO_x in the dark at 5 mA cm⁻². The vertical and horizontal dotted lines (gray) are for convenient comparison of OER activities of all electrodes at the equilibrium potential for water oxidation and the potential needed to reach the current density of 5 mA cm⁻²

The electrocatalytic (EC) activity of aM (M=Fe, Co, Ni) with and without FeOOH overlayer was evaluated using the heavily doped p⁺⁺-Si/SiO_x anodes as a conductive electrode²⁻⁴ in our work (Figure S10), and the specific activity comparison is also stated below.

At 1.8 $V_{\rm RHE}$, the order of the current density (mA cm⁻²): aNi:FeOOH (25.02) > aNi (21.35) > aFe:FeOOH (9.98) > aCo (7.96) > aFe (5.48) > aCo:FeOOH (0.61). At 5 mA cm⁻², the overpotential ($V_{\rm RHE}$): aNi:FeOOH (1.57) < aNi (1.60) < aFe:FeOOH (1.68) < aCo (1.74) < aFe (1.80) < aCo:FeOOH (2.23). These EC activity is consistent with that of PEC (Figure 2 and S10) of n⁺p-Si/SiO_x/aM with and without FeOOH.

At 2.0 $V_{\rm RHE}$, the order of the current density (mA cm⁻²): aNi:FeOOH (44.93) > aNi (38.21) > aFe:FeOOH (18.78) > aFe (16.48) > aCo (15.82) > aCo:FeOOH (2.15), which is not completely consistent with that of PEC of n⁺p-Si/SiO_x/aM with and without FeOOH at 2.0 $V_{\rm RHE}$. Due to 2.0 $V_{\rm RHE}$ is too high to use for the normal PEC test, we can conclude that the activity of EC for the p⁺⁺-Si/SiO_x/aM (M=Fe, Co, Ni) with and without FeOOH overlayer is consistent with that of the PEC for the n⁺p-Si/SiO_x/aM photoanode with and without FeOOH in the commonly used bias range.

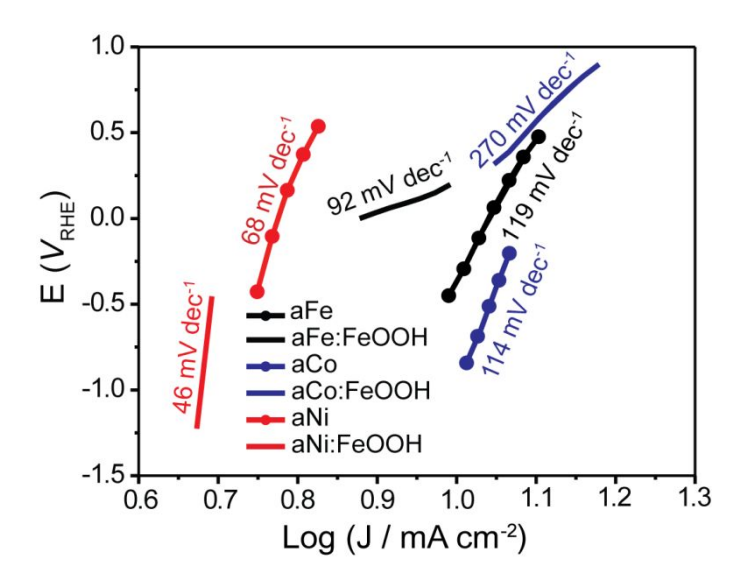


Figure S11. Tafel plots of the n⁺p-Si/SiO_x/aM (M=Fe, Co, Ni) photoanodes with and without the FeOOH overlayer extracted from the J-V plots in non-Faradaic region.

The fast electron transfer kinetics is one of key requisites of an efficient PEC performance. The influence of with and without FeOOH overlayers on OER kinetics for n⁺p-Si/SiO_x/aM photoanodes was evaluated by Tafel plots (Figure S11, Table 1). The Tafel slope of the n⁺p-Si/SiO_x/aNi:FeOOH photoanode (46 mV dec⁻¹) was remarkably lower than those of n⁺p-Si/SiO_x/aFe:FeOOH (92 mV dec⁻¹) and n⁺p-Si/SiO_x/aCo:FeOOH (270 mV dec⁻¹), fastest OER kinetics in n⁺p-Si/SiO_x/aNi:FeOOH illustrating the among Without the FeOOH overlayer, the Tafel slope of the n⁺p-Si/SiO_x/aNi photoanode (68 mV dec⁻¹) remarkably lower than those of n⁺p-Si/SiO_x/aCo (114 mV dec⁻¹) and n⁺p-Si/SiO_x/aFe (119 mV dec⁻¹), illustrating the fastest OER kinetics in n⁺p-Si/SiO_x/aNi. Moreover, in dec⁻¹ for comparison with Tafel slope of 68 n⁺p-Si/SiO_x/aNi, the mV

n⁺p-Si/SiO_x/aNi:FeOOH exhibited a smaller Tafel slope of (46 mV dec⁻¹) indicating its higher catalytic activity due to the introduction of FeOOH electrocatalyst. The smaller Tafel slope of n⁺p-Si/SiO_x/aNi:FeOOH indicates a higher enhancement in the PEC OER activity because the current density increases with the faster the overpotential. Tafel plots (Figure S11) estimated from J-V curves (Figure 2) show that the changing trend in the Tafel slope of n⁺p-Si/SiO_x/aM (M=Fe, Co, Ni) with and without the FeOOH overlayer is consistent with that in the OER activity of these anodes (Table 1, Figure S11). Therefore, the electrocatalytic activities (Figure S10) of the different catalyst layers are basically consistent with the PEC activities (Figure 2) of n⁺p-Si/SiO_x/aM photoanodes with and without FeOOH.

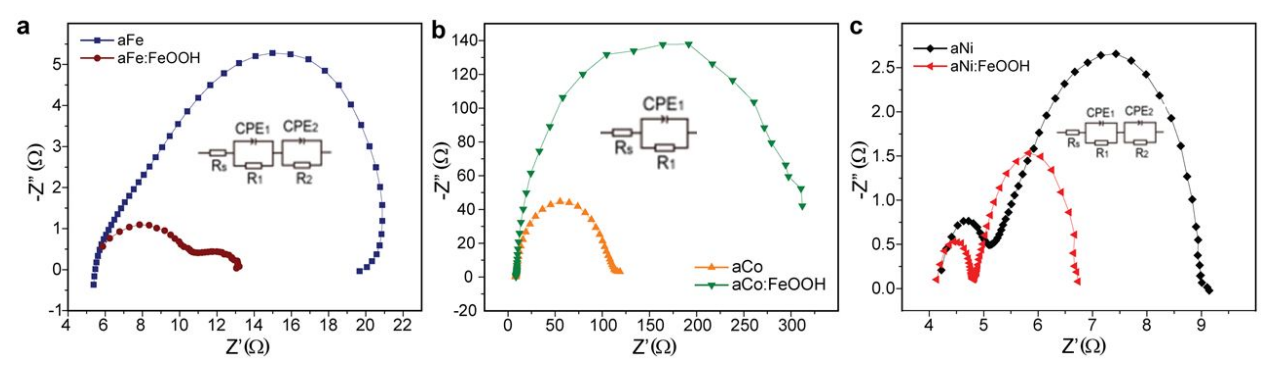


Figure S12. Impedance Nyquist plots of aFe and aFe:FeOOH (a); aCo and aCo:FeOOH (b); aNi and aNi:FeOOH (c) coated on n^+p -Si/SiO_x photoanodes measured at 1.23 V_{RHE} under 1 sun irradiation.

Impedance Nyquist plots were analyzed by fitting to the equivalent electronic circuit model using ZSimpWin software illustrated in Figure S12. In the two-arc equivalent circuit (Figure S12a, S12c), R_s denotes solution resistance of the photoanode system, CPE₁ and CPE₂ represent constant phase elements; R_I and R_2 represent the resistances of charge transfer at the photoanode/electrolyte interface and in the photoanode bulk, respectively. The first semicircle on the left appearing at the high-frequency region corresponds to R_I which is related to the kinetics of water oxidation, while the second semicircle on the right at the low-frequency region corresponds to R_2 . The interfacial charge transfer series resistance ($R_I + R_2$) represents the charge transfer resistance both in the photoanode bulk (R_I) and at the photoanode/electrolyte interface (R_2) at the PEC DC operation current. As shown in Figure S12b, in single-arc circuit R_s represents the solution resistance; the capacitance CPE and

resistance R_I characterize the charge-transfer behavior across the electrode/electrolyte interface.³¹

Table S7. EIS parameters for n⁺p-Si/SiO_x/aM (M=Fe, Co, Ni) with and without the FeOOH overlayer

Photoanode	Interfacial resistance (Ω)	$egin{array}{c} R_1 \ (\Omega) \end{array}$	$egin{array}{c} R_2 \ (\Omega) \end{array}$
aFe	14.29	14.29	
aFe:FeOOH	7.19	5.15	2.04
aCo	11.06	11.06	
aCo:FeOOH	308.37	308.37	
aNi	4.93	0.88	4.05
aNi:FeOOH	2.60	0.67	1.93

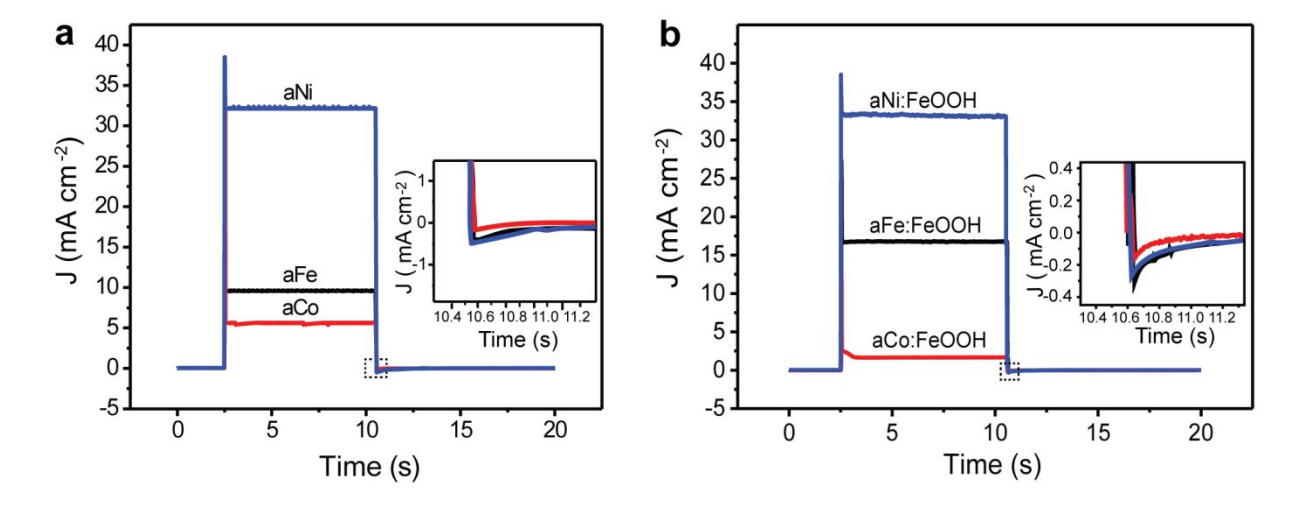


Figure S13. Chopped light chronoamperometry measurements for (a) $n^+p-Si/SiO_x/aM$ and (b) $n^+p-Si/SiO_x/aM$: FeOOH photoanodes (M=Fe, Co, Ni). Inset is the zoomed-in area of the negative current transient region.

To evaluate the hole accumulation ability of the n^+p -Si/SiO_x/aM (M=Fe, Co, Ni) photoanodes with and without the FeOOH overlayer, we used a transient photocurrent surface charging-discharging method to test the density of the accumulated holes under steady-state conditions during the OER at 1.23 $V_{\rm RHE}$. When the light is turned on, the anodic spike in photocurrent reaches to the steady-state current density. When the light is turned off, the cathodic spike in current quickly decays to the steady dark current owing to recombination of the continuing flux of electrons to the surface stored holes. These spikes have been attributed to the charging (trapping of holes) and discharging of surface states or oxidizing and reducing surface species. Thus the surface hole accumulation capacity (Q) under OER condition (Figure 3d) can be calculated by integrating the J-t plots (Figure S13) within the negative current transient regions. 33,34

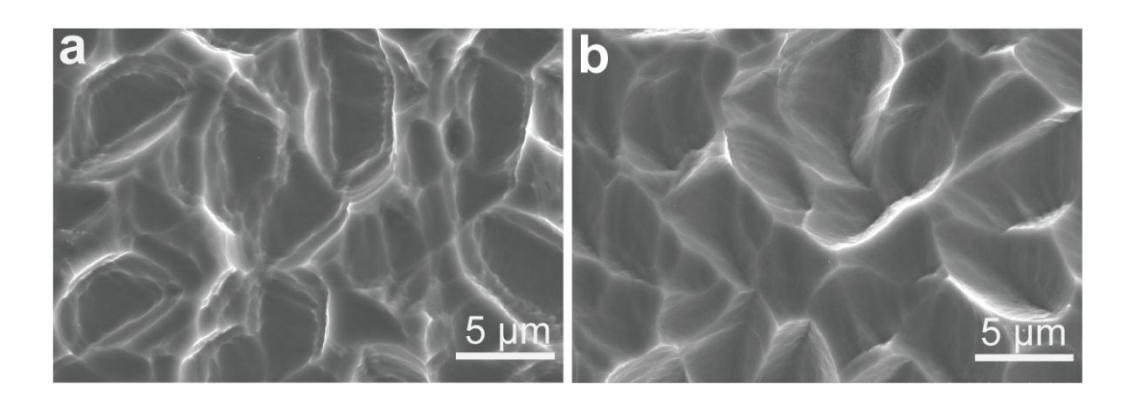


Figure S14. SEM images of n⁺p-Si/SiO_x/aNi:FeOOH (a) before and (b) after the stability test. The morphology of the Si substrate surface after the stability test was obtained by removing aNi:FeOOH using diluted hydrochloric acid, and basically keeps intact.

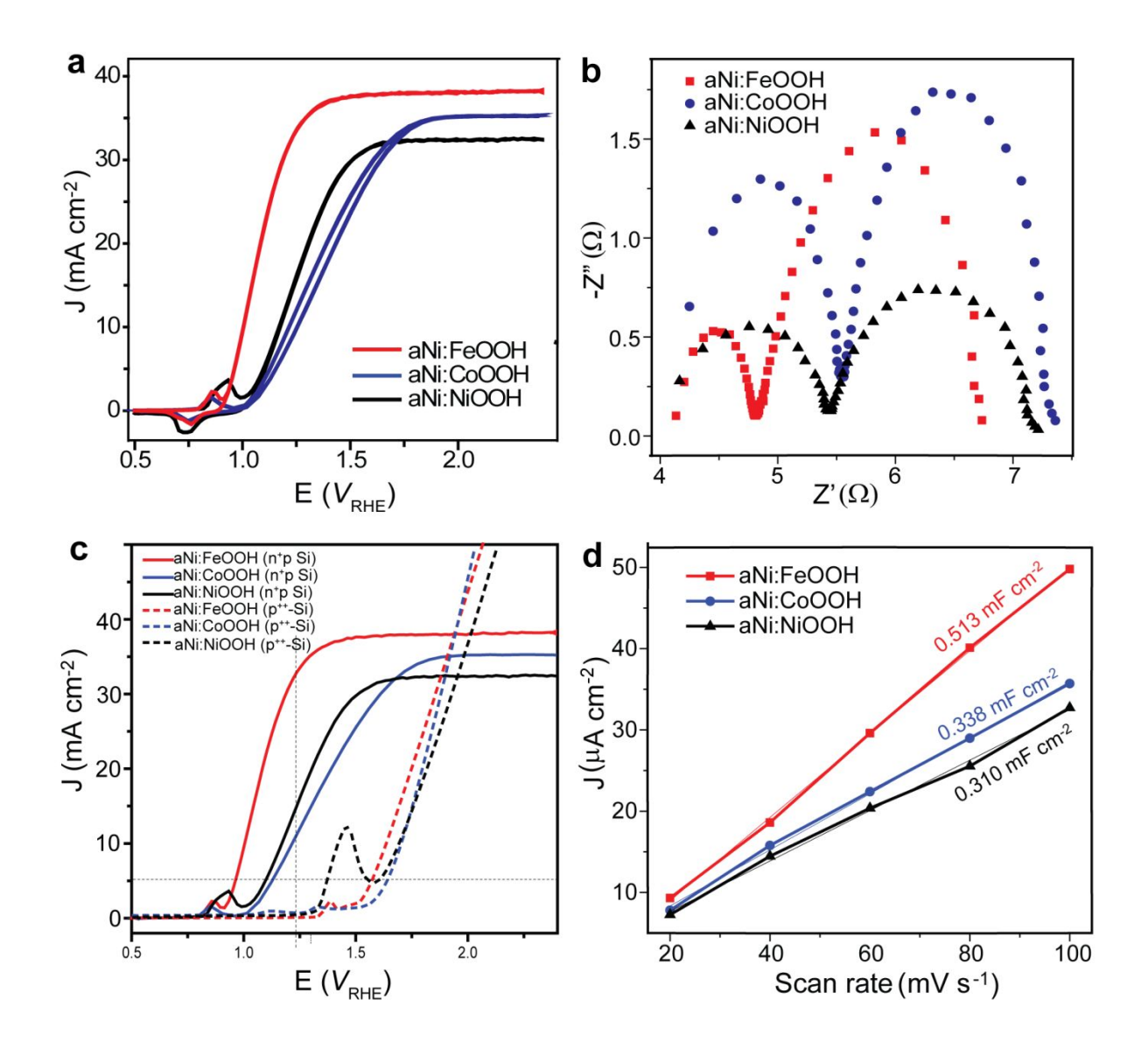


Figure S15. Cyclic voltammetry measurements at the scan rate of 50 mV s⁻¹ (a); impedance Nyquist plots measured at 1.23 $V_{\rm RHE}$ (b); photovoltage at the scan rate of 50 mV s⁻¹ (c); and capacitive currents at different scan rates (d); for the optimized n⁺p-Si/SiO_x/aNi:MOOH (M= Fe, Co, Ni) photoanodes conducted in 1 M KOH electrolyte under irradiation of 100 mW cm⁻² (AM 1.5 G).

Table S8. Test parameters for n⁺p-Si/SiO_x/aNi:MOOH (M=Fe, Co, Ni) photoanodes

Photoanode	Onset potential $(V_{\rm RHE})$	Photocurrent density at 1.23 $V_{ m RHE}$	Saturation photocurrent density (mA cm ⁻²)	Potential at 5 mA cm ⁻²	EIS Interfa cial resista nce (Ω)	R_1 (Ω)	$egin{array}{c} R_2 \ (\Omega) \end{array}$	Photo voltage (mV _{RHE})	ECSA (mF cm ⁻²)
aNi:FeOOH	0.91	33.20	38.50	0.99	2.60	0.67	1.93	610	0.513
aNi:CoOOH	0.94	11.53	35.27	1.13	3.12	1.32	1.80	510	0.338
aNi:NiOOH	1.00	15.94	32.51	1.10	3.04	1.28	1.76	500	0.310

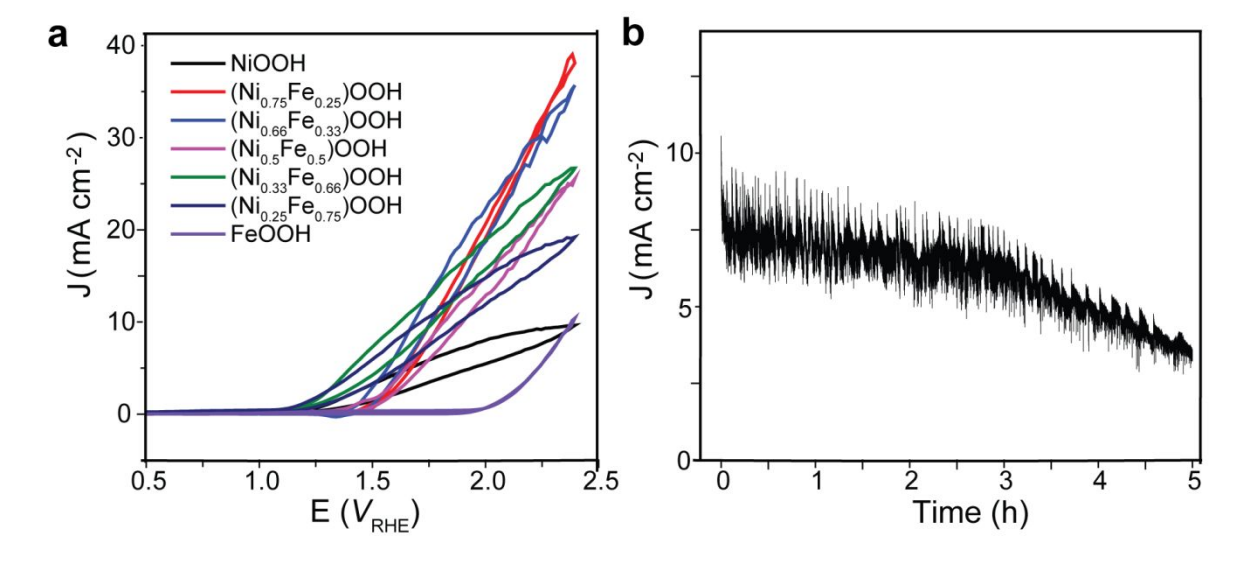


Figure S16. (a) Cyclic voltammetry measurements of n^+p -Si/SiO_x/(Ni_{1-x}Fe_x)OOH photoanodes at the scan rate of 50 mV s⁻¹, with n^+p -Si/SiO_x/NiOOH and n^+p -Si/SiO_x/FeOOH photoanodes as comparison and Chronoamperometric stability response of n^+p -Si/SiO_x/(Ni_{0.33}Fe_{0.66})OOH photoanode for 5 h at 1.62 $V_{\rm RHE}$ (b); experiments conducted in 1 M KOH under irradiation of 100 mW cm⁻² (AM 1.5 G).

In addition, we deposited FeOOH and Ni_{1-x}Fe_xOOH directly on n⁺p-Si/SiO_x without the aNi interlayer as control samples. The n⁺p-Si/SiO_x/FeOOH photoanode performance is really poor with an onset potential of ~1.98 $V_{\rm RHE}$ and a low current density of ~79 μ A cm⁻² at 1.23 $V_{\rm RHE}$ (Figure 2 and Figure S16a). The optimized n⁺p-Si/SiO_x/(Ni_{0.33}Fe_{0.66})OOH photoanode with a dual metal element EC has better PEC performance with an onset potential of ~1.2 $V_{\rm RHE}$ and a current density of ~1.28 mA cm⁻² at 1.23 $V_{\rm RHE}$ (Figure S16a). The chronoamperometry test of the n⁺p-Si/SiO_x/(Ni_{0.33}Fe_{0.66})OOH photoanode displays a rapid current density decay to half of the original value after 5 h (Figure S16b).

References

- (1) Chen, J.; Xu, J.; Zhou, S.; Zhao, N.; Wong, C. P. Amorphous Nanostructured FeOOH and Co-Ni Double Hydroxides for High-Performance Aqueous Asymmetric Supercapacitors. *Nano Energy* **2016**, *21*, 145–153.
- (2) Zhou, X.; Liu, R.; Sun, K.; Papadantonakis, K. M.; Brunschwig, B. S.; Lewis, N. S. 570 mV Photovoltage, Stabilized n-Si/CoO_x Heterojunction Photoanodes Fabricated Using Atomic Layer Deposition. *Energy Environ. Sci.* **2016**, *9* (3), 892–897.
- (3) Oh, S.; Jung, S.; Lee, Y. H.; Song, J. T.; Kim, T. H.; Nandi, D. K.; Kim, S.-H.; Oh, J. Hole-Selective CoO_x/SiO_x/Si Heterojunctions for Photoelectrochemical Water Splitting. *ACS Catal.* **2018**, *8* (10), 9755–9764.
- (4) Guo, B.; Batool, A.; Xie, G.; Boddula, R.; Tian, L.; Jan, S. U.; Gong, J. R. Facile Integration between Si and Catalyst for High-Performance Photoanodes by a Multifunctional Bridging Layer. *Nano Lett.* **2018**, *18* (2), 1516–1521.
- (5) Cai, L.; Zhao, J.; Li, H.; Park, J.; Cho, I. S.; Han, H. S.; Zheng, X. One-Step Hydrothermal Deposition of Ni:FeOOH onto Photoanodes for Enhanced Water Oxidation. *ACS Energy Lett.* **2016**, *1* (3), 624–632.
- (6) Liu, A.; Liu, J.; Pan, B.; Zhang, W. Formation of Lepidocrocite (γ-FeOOH) from Oxidation of Nanoscale Zero-Valent Iron (NZVI) in Oxygenated Water. RSC Adv. 2014, 4 (101), 57377–57382.
- (7) Zhou, H.; Yu, F.; Zhu, Q.; Sun, J.; Qin, F.; Yu, L.; Bao, J.; Yu, Y.; Chen, S.; Ren, Z. Water Splitting by Electrolysis at High Current Densities under 1.6 Volts. *Energy Environ. Sci.* **2018**, *11* (10), 2858–2864.
- (8) Li, C.; Xiao, Y.; Zhang, L.; Li, Y.; Delaunay, J.-J.; Zhu, H. Efficient Photoelectrochemical Water Oxidation Enabled by an Amorphous Metal Oxide-Catalyzed Graphene/Silicon Heterojunction Photoanode. *Sustain. Energy Fuels* **2018**, *2*, 663–672.
- (9) Yu, X.; Yang, P.; Chen, S.; Zhang, M.; Shi, G. NiFe Alloy Protected Silicon Photoanode for Efficient Water Splitting. *Adv. Energy Mater.* **2017**, *7* (6), 1–6.
- (10) Loget, G.; Fabre, B.; Fryars, S.; Mériadec, C.; Ababou-Girard, S. Dispersed Ni Nanoparticles Stabilize Silicon Photoanodes for Efficient and Inexpensive Sunlight-Assisted Water Oxidation. *ACS Energy Lett.* **2017**, *2* (3), 569–573.
- (11) Cai, Q.; Hong, W.; Jian, C.; Li, J.; Liu, W. Impact of Silicon Resistivity on the Performance of Silicon Photoanode for Efficient Water Oxidation Reaction. *ACS Catal.* **2017**, 7 (5), 3277–3283.
- (12) Digdaya, I. A.; Adhyaksa, G. W. P.; Trześniewski, B. J.; Garnett, E. C.; Smith, W. A. Interfacial Engineering of Metal-Insulator-Semiconductor Junctions for Efficient and Stable Photoelectrochemical Water Oxidation. *Nat. Commun.* **2017**, *8* (May), 15968.
- (13) Yoon, K.; Lee, J. H.; Kang, J.; Kang, J.; Moody, M. J.; Hersam, M. C.; Lauhon, L. J. Metal-Free Carbon-Based Nanomaterial Coatings Protect Silicon Photoanodes in Solar

- Water-Splitting. Nano Lett. 2016, 16 (12), 7370-7375.
- (14) Bae, D.; Mei, B.; Frydendal, R.; Pedersen, T.; Seger, B.; Hansen, O.; Vesborg, P. C. K.; Chorkendorff, I. Back-Illuminated Si-Based Photoanode with Nickel Cobalt Oxide Catalytic Protection Layer. *ChemElectroChem* **2016**, *3* (10), 1517.
- (15) Scheuermann, A. G.; Lawrence, J. P.; Kemp, K. W.; Ito, T.; Walsh, A.; Chidsey, C. E. D.; Hurley, P. K.; McIntyre, P. C. Design Principles for Maximizing Photovoltage in Metal-Oxide-Protected Water-Splitting Photoanodes. *Nat. Mater.* 2016, *15* (1), 99–105.
 (16) Yang, J.; Walczak, K.; Anzenberg, E.; Toma, F. M.; Yuan, G.; Beeman, J.; Schwartzberg, A.; Lin, Y.; Hettick, M.; Javey, A.; et al. Efficient and Sustained Photoelectrochemical Water Oxidation by Cobalt Oxide/Silicon Photoanodes with Nanotextured Interfaces. *J. Am. Chem. Soc.* 2014, *136* (17), 6191–6194.
- (17) Chen, L.; Yang, J.; Klaus, S.; Lee, L. J.; Woods-Robinson, R.; Ma, J.; Lum, Y.; Cooper, J. K.; Toma, F. M.; Wang, L.-W.; et al. P-Type Transparent Conducting Oxide/n-Type Semiconductor Heterojunctions for Efficient and Stable Solar Water Oxidation. *J. Am. Chem. Soc.* **2015**, *137* (30), 9595–9603.
- (18) Hill, J. C.; Landers, A. T.; Switzer, J. A. An Electrodeposited Inhomogeneous Metal-Insulator-Semiconductor Junction for Efficient Photoelectrochemical Water Oxidation. *Nat. Mater.* **2015**, *14* (11), 1150–1155.
- (19) Kenney, M. J.; Gong, M.; Li, Y.; Wu, J. Z.; Feng, J.; Lanza, M.; Dai, H. High-Performance Silicon Photoanodes Passivated with Ultrathin Nickel Films for Water Oxidation. *Science* **2013**, *342* (6160), 836–840.
- (20) Sun, K.; McDowell, M. T.; Nielander, A. C.; Hu, S.; Shaner, M. R.; Yang, F.; Brunschwig, B. S.; Lewis, N. S. Stable Solar-Driven Water Oxidation to O₂(G) by Ni-Oxide-Coated Silicon Photoanodes. *J. Phys. Chem. Lett.* **2015**, *6* (4), 592–598.
- (21) Sun, K.; Saadi, F. H.; Lichterman, M. F.; Hale, W. G.; Wang, H.-P.; Zhou, X.; Plymale, N. T.; Omelchenko, S. T.; He, J.-H.; Papadantonakis, K. M.; et al. Stable Solar-Driven Oxidation of Water by Semiconducting Photoanodes Protected by Transparent Catalytic Nickel Oxide Films. *Proc. Natl. Acad. Sci.* **2015**, *112* (12), 3612–3617.
- (22) Mei, B.; Permyakova, A. a; Frydendal, R.; Bae, D.; Pedersen, T.; Malacrida, P.; Hansen, O.; Stephens, I. E. L.; Vesborg, P. C. K.; Seger, B.; et al. Iron-Treated NiO as a Highly Transparent P-Type Protection Layer for Efficient Si-Based Photoanodes. *J. Phys. Chem. Lett.* **2014**, *5* (20), 3456–3461.
- (23) Lee, S. A.; Lee, T. H.; Kim, C.; Lee, M. G.; Choi, M.-J.; Park, H.; Choi, S.; Oh, J.; Jang, H. W. Tailored NiO_x/Ni Cocatalysts on Silicon for Highly Efficient Water Splitting Photoanodes via Pulsed Electrodeposition. *ACS Catal.* **2018**, *8*, 7261–7269.
- (24) Zhao, J.; Gill, T. M.; Zheng, X. Enabling Silicon Photoanodes for Efficient Solar Water Splitting by Electroless-Deposited Nickel. *Nano Res.* **2018**, *11* (6), 3499–3508.
- (25) Hu, S.; Shaner, M. R.; Beardslee, J. A.; Lichterman, M.; Brunschwig, B. S.; Lewis, N. S. Amorphous TiO₂ Coatings Stabilize Si, GaAs, and GaP Photoanodes for Efficient Water Oxidation. *Science* **2014**, *344* (6187), 1005–1009.

- Mei, B.; Seger, B.; Pedersen, T.; Malizia, M.; Hansen, O.; Chorkendorff, I.; Vesborg, P.
 C. K. Protection of P⁺-n-Si Photoanodes by Sputter-Deposited Ir/IrO_x Thin Films. *J. Phys. Chem. Lett.* 2014, 5 (11), 1948–1952.
- (27) Chen, Y. W.; Prange, J. D.; Dühnen, S.; Park, Y.; Gunji, M.; Chidsey, C. E. D.; McIntyre, P. C. Atomic Layer-Deposited Tunnel Oxide Stabilizes Silicon Photoanodes for Water Oxidation. *Nat. Mater.* **2011**, *10* (7), 539–544.
- (28) Li, C.; Huang, M.; Zhong, Y.; Zhang, L.; Xiao, Y.; Zhu, H. Highly Efficient NiFe Nanoparticle Decorated Si Photoanode for Photoelectrochemical Water Oxidation. *Chem. Mater.* **2019**, *31* (1), 171–178.
- (29) Moreno-Hernandez, I. A.; Brunschwig, B. S.; Lewis, N. S. Tin Oxide as a Protective Heterojunction with Silicon for Efficient Photoelectrochemical Water Oxidation in Strongly Acidic or Alkaline Electrolytes. *Adv. Energy Mater.* **2018**, *8* (24), 1801155.
- (30) Cai, Q.; Hong, W.; Jian, C.; Li, J.; Liu, W. Insulator Layer Engineering toward Stable Si Photoanode for Efficient Water Oxidation. *ACS Catal.* **2018**, *8* (10), 9238–9244.
- (31) Zhang, B.; Wang, L.; Zhang, Y.; Ding, Y.; Bi, Y. Ultrathin FeOOH Nanolayers with Abundant Oxygen Vacancies on BiVO₄ Photoanodes for Efficient Water Oxidation. *Angew. Chemie Int. Ed.* **2018**, *57* (8), 2248–2252.
- (32) Lin, F.; Boettcher, S. W. Adaptive Semiconductor/Electrocatalyst Junctions in Water-Splitting Photoanodes. *Nat. Mater.* **2014**, *13* (1), 81–86.
- (33) Cui, C.; Heggen, M.; Zabka, W.; Cui, W.; Osterwalder, J.; Probst, B.; Alberto, R. Atomically Dispersed Hybrid Nickel-Iridium Sites for Photoelectrocatalysis. *Nat. Commun.* **2017**, *8* (1), 1341.
- (34) Klahr, B.; Gimenez, S.; Fabregat-Santiago, F.; Bisquert, J.; Hamann, T. W. Electrochemical and Photoelectrochemical Investigation of Water Oxidation with Hematite Electrodes. *Energy Environ. Sci.* **2012**, *5* (6), 7626–7636.